Journal of Advanced Ceramics
2024, **13**(10): 1590–1599
https://doi.org/10.26599/JAC.2024.9220959

Research Article

Nb-doped $PrBa_{0.8}Ca_{0.2}Co_2O_6$-based perovskite cathode with improved oxygen reduction reaction activity and stability for solid oxide fuel cells

Depeng Zeng, Feng Zhu, Kang Xu, Hua Zhang, Yangsen Xu, Yu Chen✉

School of Environment and Energy, South China University of Technology, Guangzhou 510006, China

Received: May 21, 2024; Revised: July 25, 2024; Accepted: August 14, 2024

Abstract: The performance of a solid oxide fuel cell (SOFC) is strongly associated with the activity and durability of the cathode, where the oxygen reduction reaction occurs. In this study, we report our findings in the development of an Nb-doped $PrBa_{0.8}Ca_{0.2}Co_2O_{6-\delta}$ ($PrBa_{0.8}Ca_{0.2}Co_{2-x}Nb_xO_{6-\delta}$, x = 0, 0.025, 0.05, and 0.1, denoted as $PBCCN_x$) perovskite composite as the SOFC cathode. Analyses of X-ray diffraction (XRD) patterns and energy-dispersive transmission electron microscopy (TEM-EDS) images suggest that after being treated at 950 °C in air, $PBCCN_{0.05}$ mainly contains phases of Ca- and Nb-doped $PrBaCo_2O_{6-\delta}$ double perovskite, $PrCoO_3$ perovskite with Ca and Nb doping, and $Ba_3Ca_{1.18}Nb_{1.82}O_{9-\delta}$. When evaluated as an SOFC cathode, the $PBCCN_{0.05}$ mixture has shown a low polarization resistance of 0.0074 Ω·cm² at 800 °C in $La_{0.8}Sr_{0.2}Ga_{0.8}Mg_{0.2}O_3$ electrolyte symmetrical cells. Accordingly, anode-supported single cells with a configuration of Ni–$Zr_{0.84}Y_{0.16}O_{2-\delta}$ (YSZ)/YSZ/$Gd_{0.1}Ce_{0.9}O_{2-\delta}$/$PBCCN_{0.05}$ display high electrochemical performance, with a peak power density of 1.81 W·cm^{-2} and a reasonable durability of 100 h at 800 °C. $PBCCN_{0.05}$ possesses a higher concentration of oxygen vacancies, a faster oxygen surface adsorption–dissociation rate, and an increased mass ratio of $PrCoO_3$ perovskite with Ca and Nb doping compared to $PrBa_{0.8}Ca_{0.2}Co_2O_{6-\delta}$ without Nb doping.

Keywords: self-assembly; Nb doping; cathodes; oxygen reduction reactions; solid oxide fuel cells (SOFCs)

1 Introduction

Currently, increasing extreme climate phenomena, greenhouse gas emissions, and environmental pollution have become urgent problems [1–7] that compel society to reduce its dependence on fossil fuels for further development [8,9], and much attention has been focused on reversible energy and pollution-free power generation [10–15]. Solid oxide fuel cells (SOFCs), as possible candidates in this situation, can both operate reversibly and directly transfer chemical energy into electricity through the electro-oxidation of fuel without the intermediate step of combustion. Thus, SOFCs can eliminate the limit from Carnot cycle efficiency, and have received a significant amount of attention as a plausible solution for the extensive application of stationary power generation [16,17].

The oxygen reduction reaction (ORR) occurring at the cathode is an essential step for SOFCs; thus, numerous studies have focused on finding suitable materials with high electrochemical performance. As a pivotal type of material in SOFCs, perovskite-type oxides have shown tremendous prospects in the electrocatalysis of ORR at the cathode of SOFCs [18–22]. Perovskite materials such as simple perovskite (for example, $La_{0.6}Sr_{0.4}Co_{0.2}Fe_{0.8}O_{3-\delta}$ [23–25], $Ba_{0.5}Sr_{0.5}Co_{0.8}Fe_{0.2}O_{3-\delta}$ [26–28], etc.) and double perovskite (for instance, $PrBaCo_2O_{5+\delta}$ [29]) have been investigated. However, increasing the performance, especially the peak power density and durability of SOFCs, is still needed to develop better cathode materials with excellent ORR activity and good stability for practical applications. $PrBaCo_2O_{5+\delta}$-type double perovskites are reported to have many oxygen vacancies, forming a facile pathway for the rapid diffusion of oxygen ions [30]. Therefore, it has demonstrated superior electrochemical performance and has become an ideal baseline material for researchers seeking more advanced cathode materials in recent years [31–35].

To achieve this goal, doping at the A or B site of $PrBaCo_2O_{5+\delta}$ is an effective way to enhance the electrochemical properties of the cathode of an SOFC. For example, a Ca-doped double perovskite $PrBa_{0.8}Ca_{0.2}Co_2O_{5+\delta}$ (PBCC) cathode showed an excellent peak power density of 0.949 W·cm^{-2} at 700 °C and stable operation of an SOFC with a PBCC cathode under 1% CO_2 conditions [36]. Lim *et al.* [37] reported Fe-doped $PrBa_{0.8}Ca_{0.2}Co_{1.5}Fe_{0.5}O_{5+\delta}$ (PBCCF05) cathode materials with a low polarization resistance (R_p) of 0.080 Ω·cm² and an incredible peak power density of 1.89 W·cm^{-2} at 600 °C, suggesting that Fe doping is a useful strategy for facilitating ORR activity. Furthermore, partial substitution of Co by Fe can reduce the thermal expansion coefficient of PBCCF05 and result in better long-term stability under fuel cell operating conditions. Moreover, surface decoration is also an effective method because of its relatively simple process and low cost. Zhang *et al.* [38] reported the successful synthesis of a $Gd_{0.1}Ce_{0.9}O_{2-\delta}$-decorated $PrBaCo_2O_{5+\delta}$ composite (PBC–10 wt% GDC) via a one-pot method, which resulted in 78% lower polarization resistance (0.394 Ω·cm²) than that of a bare PBC cathode in symmetrical cells. Zhou *et al.* [39] reported the

✉ Corresponding author.
E-mail: eschenyu@scut.edu.cn

formation of a BCO-decorated PBCC air electrode (PBCC-BCO) when a pure PBCC reacts with water under typical protonic ceramic electrolysis cell conditions (high steam concentration); the cells achieved a peak power density of 1.06 W·cm^{-2}, indicating that surface decoration could be a successful method for increasing the electrochemical performance.

Here, we report our findings concerning the development of SOFC cathodes by doping Nb at the B site of the $PrBa_{0.8}Ca_{0.2}Co_2O_{6-\delta}$ (PBCC) perovskite, which has a designed formula of $PrBa_{0.8}Ca_{0.2}Co_{1.95}Nb_{0.05}O_{6-\delta}$ ($PBCCN_{0.05}$). However, after calcination at 950 °C in air, $PBCCN_{0.05}$ mainly self-assembled and decomposed into phases, which were possibly Ca- and Nb-doped $PrBaCo_2O_{6-\delta}$ double perovskite, the $PrCoO_3$ perovskite with Ca and Nb doping and the $Ba_3Ca_{1.18}Nb_{1.82}O_{9-\delta}$ phase. The oxygen surface adsorption–dissociation step of ORR is accelerated on the $PBCCN_{0.05}$ surface, which results in improved ORR activity. The $PBCCN_{0.05}$ cathode has displayed a low R_p of 0.0074 Ω·cm^2 in a symmetrical cell, a high peak power density of 1.81 W·cm^{-2}, and reasonable durability of 100 h in a single cell at 800 °C.

2 Experimental

2.1 Powder synthesis

The Nb-doped PBCC powders ($PrBa_{0.8}Ca_{0.2}Co_{2-x}Nb_xO_{6-\delta}$, x = 0, 0.025, 0.05, and 0.1, denoted $PBCCN_x$) were synthesized via the solution combustion method. First, the raw materials $Pr(NO_3)_3{\cdot}6H_2O$, $Ba(NO_3)_2$, $Ca(NO_3)_2$, $Co(NO_3)_2{\cdot}6H_2O$, and $C_2H_5NNbO_4$ were dissolved in deionized water at a stoichiometric ratio of 1 : 0.8 : 0.2 : (2–x) : x (x = 0, 0.25, 0.5, and 0.1). After that, complexing agents of citric acid and glycine were added to the solution at the same molar ratio of 1 : 0.75 for total metal ions : complexing agents. The solution was continuously stirred and heated at 90 °C until gelation. The gel was subsequently heated to 250 °C in an oven and turned into ash after total combustion, after which it was then heated at 950 °C for 2 h in air. For convenience, the sample without Nb doping is denoted as PBCC.

The $La_{0.8}Sr_{0.2}Ga_{0.8}Mg_{0.2}O_3$ (LSGM) powder was fabricated via a solid-state reaction process. La_2O_3 and MgO were calcined at 1000 °C for 2 h to eliminate moisture and organic species before weighing. Then, La_2O_3, $SrCO_3$, Ga_2O_3, and MgO were mixed in absolute ethanol at stoichiometric amounts and ball-milled for 24 h via zirconia balls of 6 mm in diameter in a planetary ball mill. After being thoroughly dried, the mixture was calcined at 1250 °C for 5 h. NiO, $Zr_{0.84}Y_{0.16}O_{2-\delta}$ (YSZ), and $Gd_{0.1}Ce_{0.9}O_{2-\delta}$ (GDC) powders were purchased from H2-BANK.

2.2 Cell fabrication

The $PBCCN_x$ ink (x = 0, 0.025, 0.05, and 0.1) for screen printing was made by mixing the M-$PBCCN_x$ powder, ethyl cellulose, and terpinol in an agate mortar at a weight ratio of 1 : 0.04 : 0.76 and grinding for 1 h in an agate mortar. The LSGM electrolyte for symmetrical cells was made by pressing the LSGM powder into compacted pellets with a diameter of approximately 10 mm. The pellets were then calcined at 1450 °C for 5 h to obtain a sufficiently high density. After that, the $PBCCN_x$ ink was screen-printed on both sides of the LSGM electrolyte pellets and calcined at 950 °C for 2 h to form $PBCCN_x$/LSGM/$PBCCN_x$ symmetrical cells. The active area of the $PBCCN_x$ cathode is approximately 0.2826 cm^2. Ni–$Zr_{0.84}Y_{0.16}O_{2-\delta}$ (Ni–YSZ) anode-supported half-cells were fabricated via tape casting and co-sintering. Co-tape casting and co-sintering methods were employed to fabricate anode-supported single cells. The electrolyte slurry was obtained by ball-milling 6 g of YSZ powder in an organic solution (5.74 g) for 48 h. The organic solution consisted of absolute ethanol and butyl acetate as the solvent, fish oil as the dispersant, PAG as the lubricant, benzyl butyl phthalate as the plasticizer, and polyvinyl butyral as the binder. The anode functional layer slurry was a mixture of 3.6 g NiO, 2.4 g YSZ, 0.6 g graphite (used as a pore-making agent), and 6.69 g organic solution after being ball-milled for 48 h. The anode-supported layer slurry was prepared by mixing 30 g NiO, 20 g YSZ, 12 g graphite (used as a pore-making agent), 8 g starch (used as a pore-making agent), and 32.2 g organic solution, followed by ball-milling for 48 h. Then, slurries of the electrolyte, anode functional layer, and anode were cast layer by layer on a polymer film. After 15 h of drying in air, the tape was punched into pellets and then preheated at 600 °C for 2 h to eliminate organic additives. A slow heating of 1 °C·min^{-1} was applied to avert any cracks in the pellets. These three-layered stacking pellets were finally co-sintered at 1400 °C for 5 h to form anode-supported half cells, which are approximately 12 mm in diameter and 0.6 mm in thickness. After that, a GDC suspension composed of GDC powder, ethyl cellulose, terpinol, and acetone with a mass ratio of 1 : 0.15 : 1.85 : 10 was drop-coated on the surface of the YSZ electrolyte and then sintered at 1300 °C for 2 h to form a GDC buffer layer. $PBCCN_x$ cathodes on single cells were made via the same method as those on LSGM symmetrical cells.

2.3 Characterizations and cell testing

The crystal structure of the $PBCCN_x$ powders was determined via an X-ray diffractometer (XRD; D8 Advance, Bruker, Germany), with Cu used as the target material. The tube current was 40 mA, the generator voltage was 40 kV, and the scanning rate was 3 (°)·min^{-1}. The XRD Rietveld refinement of PBCC and $PBCCN_{0.05}$ was carried out via the Rietveld refinement method via the GSAS (general structure analysis system) software. The XRD data of $PrBaCo_2O_{5.68}$ (JCPDF#53-0131) and $PrCoO_3$ (JCPDF#25-1069) were selected as basic structural models. The simulated polycrystalline diffraction spectrum was calculated by a specific Kurtosis function. The crystal structure parameters and Kurtosis parameters were adjusted via the least squares method to fit the real XRD spectrum and obtain the ratios of $PrBaCo_2O_{5.68}$ and $PrCoO_3$ in the samples. The microstructure of the cells was viewed by a scanning electron microscope (SEM; SU8010, Hitachi, Japan). The nanostructure and element distribution of the sample were detected by an energy-dispersive transmission electron microscope (TEM-EDS; Tecnai G2 F20, FEI, USA). The binding properties of the elements in the structure of the sample were analyzed via an X-ray photoelectron spectroscope (XPS; K-Alpha, Thermo Scientific). The deconvolution of the peak used to define each oxygen binding type was carried out via the Avantage software. Thermogravimetric (TG) measurements were performed with a TG analyzer (STA449 F3, NETZSCH, Germany) in ambient air from room temperature to 800 °C at a heating rate of 10 °C·min^{-1}. A homemade device was utilized for testing both the symmetrical cells and the single cells, as reported previously [36].

The symmetrical cells were tested at 800, 750, 700, and 650 °C in ambient air, and the cooling rate of the temperature was 2 °C·min^{-1}. For testing at different oxygen partial pressures (p_{O_2}), the cells were tested at 750 °C. The total flow rate was maintained at 100 mL min^{-1}. p_{O_2} was changed by regulating the flow rate of pure O_2 and N_2. The single cells were tested under the conditions of humidified hydrogen with 3% steam as fuel at a flow rate of 100 mL·min^{-1} and ambient air as the oxidant. Sliver wires were attached to the anode and cathode via silver paste as a current

collector during the experiment. The electrochemical impedance spectra (EIS; frequency range from 10^5 to 0.1 Hz) and current density–voltage–power density (*I*–*V*–*P*) curves were obtained via an electrochemical workstation (MC200, PARSTAT, USA).

3 Results and discussion

3.1 Structure characterizations

Figure 1(a) shows the XRD curves of the PBCCN$_x$ (x = 0, 0.025, 0.05, and 0.1) powders fired at 950 °C for 2 h in air. A comparison of the XRD curve of PBCC with that of standard diffraction cards revealed that PBCC (x = 0) we prepared in this study was not a single-phase material. Two mixed phases are easily recognized: the main phase of the $PrBaCo_2O_{5+\delta}$ double-layer perovskite and the $PrCoO_3$ perovskite phase identified by the peaks at approximately 33.3°, 41°, and 59°. The weak peak at approximately 31°–31.5° could be attributed to the $BaCoO_3$ perovskite phase according to a previous study [40]. When x increases to 0.025, no obvious change can be observed in the XRD curve. However, when x increases to 0.05, a small and isolated peak appears beside the $BaCoO_3$ perovskite peak, which is possibly $Ba_3Ca_{1.18}Nb_{1.82}O_{9-\delta}$, as elaborated in the following transmission electron microscopy (TEM) and EDS elemental mapping analysis (Fig. 2). When x reaches 0.1, the characteristic double perovskite peaks become indistinct, indicating that the phase of the $PrBaCo_2O_{5+\delta}$ double perovskite is affected by excessive Nb doping and the loss of its layered structure. To maintain the double-layered perovskite phase, the doping amount of Nb is suggested to be 0.05 or less.

To determine how Nb doping affects the phases of PBCCN$_{0.05}$, XRD Rietveld refinement is used to conduct further research on the phase contents of PBCC and PBCCN$_{0.05}$, as displayed in Figs. 1(b) and 1(c). As the isolated peaks at 31°–31.5° are too weak, the $BaCoO_3$ perovskite phase and the unidentified phase are treated as ignorable impurities. The refinement analysis of PBCC reveals that $PrBaCo_2O_{5+\delta}$ double perovskite phase accounts for 90.5 wt% of PBCC, and the $PrCoO_3$ perovskite phase accounts for 9.5 wt%. Considering the large difference in the mass ratio between these two phases in PBCC, a reasonable hypothesis can be proposed: self-assembly occurs on the PBCC ash during calcination at 950 °C, forming a $PrCoO_3$-decorated $PrBaCo_2O_{5+\delta}$ phase material with few $BaCoO_3$ impurity phases. After Nb doping (x = 0.05), the weight ratio of the $PrBaCo_2O_{5+\delta}$ double perovskite phase decreases to 87.5 wt%, whereas the weight ratio of the $PrCoO_3$ perovskite phase increases to 12.5 wt% in PBCCN$_{0.05}$. According to this result, Nb doping in PBCCN$_{0.05}$ can induce an increase in the $PrCoO_3$-related perovskite phase, which may be helpful for better electrochemical performance. The SEM micrographs of the PBCC and PBCCN$_{0.05}$ cathodes in Fig. 1(d) show their three-dimensional porous structure; many small particles can be seen sprinkled on the surface of the skeleton. Nb doping had very little effect on the morphology of the PBCCN$_{0.05}$ cathodes since the SEM images of these two cathodes were highly similar.

Figure 2 shows the TEM images and EDS elemental mapping of PBCCN$_{0.05}$. These mappings in Fig. 2(a) indicate that most of the particles contain Pr, Ba, Ca, Co, and Nb, which is possibly the

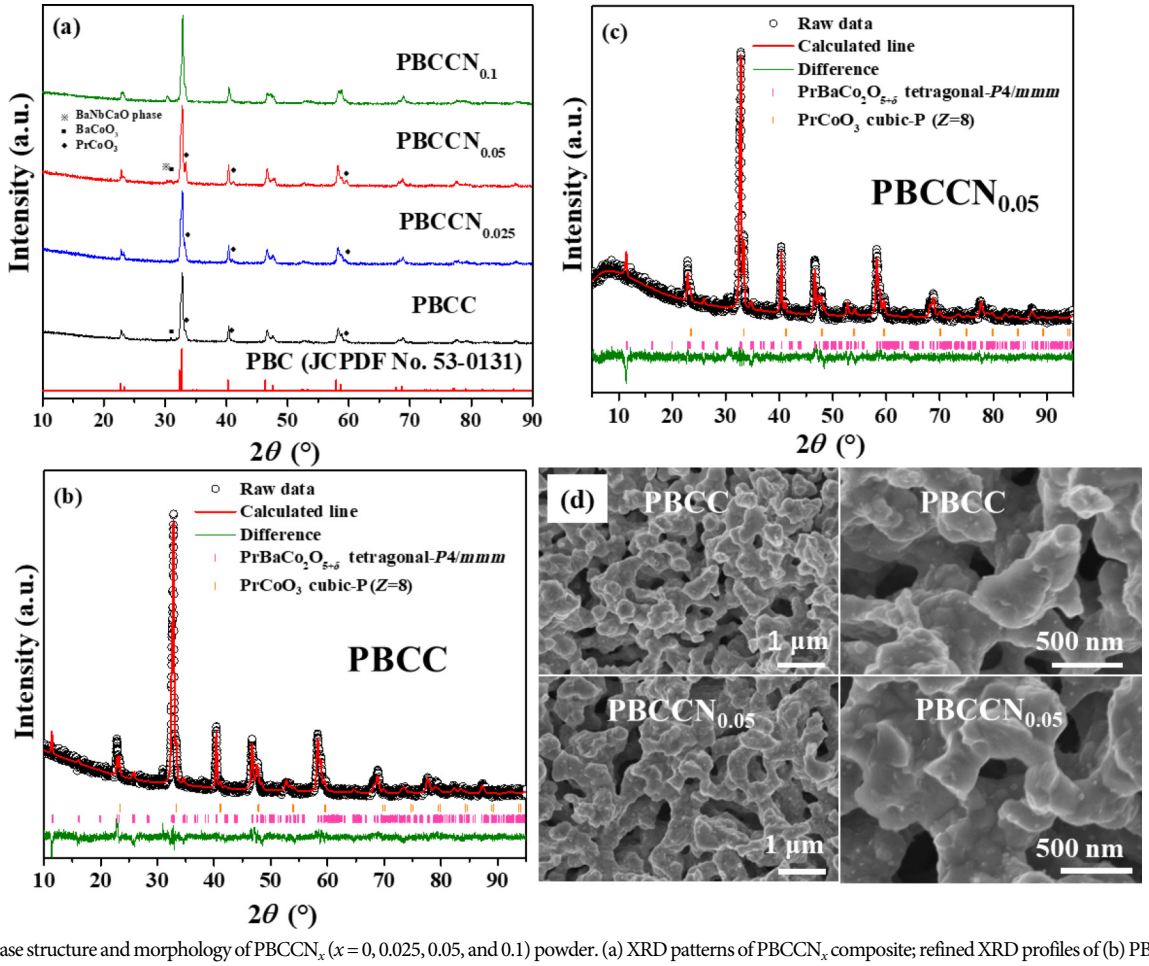

Fig. 1 Phase structure and morphology of PBCCN$_x$ (x = 0, 0.025, 0.05, and 0.1) powder. (a) XRD patterns of PBCCN$_x$ composite; refined XRD profiles of (b) PBCC (x = 0) and (c) PBCCN$_x$ (x = 0.05) powders; (d) SEM micrographs of PBCC and PBCCN$_{0.05}$.

main phase of the Ca and Nb-doped $PrBaCo_2O_{5+\delta}$ double perovskite corresponding to the XRD pattern. One obvious hole can be recognized as Ba deficiency in the Ba mapping image. At the same time, an obvious enrichment of Ca can also be observed at the same location in the particle in the Ca mapping image. Owing to the XRD refinement result of the $PBCCN_{0.05}$ structure, the phase in this region is likely to be a $PrCoO_3$ perovskite with Ca and Nb doping. Certain Nb ions are scattered on both the $PrBaCo_2O_{5+\delta}$ main phase and the $PrCoO_3$ perovskite phase, which is the proof of successful Nb doping in these two phases. Moreover, the small fragment on the upper right of the mapping images displays visible aggregation of Nb and Ba, with the absence of Pr and Co. Therefore, the phase of this small fragment could be classified as another isolated phase with Ba, Nb, and Ca in $PBCCN_{0.05}$, which should be correlated with the small and isolated peak that appears beside the $BaCoO_3$ perovskite peak in the XRD pattern of $PBCCN_{0.05}$. According to the element distribution of EDS mapping, high-resolution transmission electron microscopy (HRTEM) was used to measure the lattice fringe of each phase at the corresponding location marked in Fig. 2(b). The data of the crystal plane spacing were calculated from the average plane spacing of the 8–10 crystal planes on the corresponding phase. Three phases are found and identified in Figs. 2(c), 2(d), and 2(e). The phase in Fig. 2(d) with an interplanar spacing of 0.278 nm is similar to the (110) plane of $PrBaCo_2O_{5.68}$ (0.277 nm), and the phase in Fig. 2(e) with an interplanar spacing of 0.266 nm is close to the (220) plane of $PrCoO_3$ (0.268 nm). These results support the conclusion that the most likely phases in Figs. 2(d) and 2(e) should be the Ca- and Nb-doped $PrBaCo_2O_{6-\delta}$ double perovskite phase and the $PrCoO_3$ perovskite phase with Ca and Nb doping. The phase of the small fragment in Fig. 2(c) has an interplanar spacing of 0.295 nm. Considering the elemental composition of Ba, Nb, and Ca and the 0.295 nm interplanar spacing, we have made efforts to recognize the possible phase in Fig. 2(c) by comparing the interplanar spacing in the XRD standard card of candidate phases with 0.295 nm. Finally, the $Ba_3Ca_{1.18}Nb_{1.82}O_{9-\delta}$ phase with an interplanar spacing of the (220) plane of 0.297 nm, nearly the same as 0.295 nm, is the most likely phase in Fig. 2(c). The main peak of the $Ba_3Ca_{1.18}Nb_{1.82}O_{9-\delta}$ phase at approximately 30° is nearly the same as the isolated peak appearing beside the $BaCoO_3$ perovskite peak in $PBCCN_{0.05}$, which is likely evidence to support this possibility, and this isolated peak may come from the $Ba_3Ca_{1.18}Nb_{1.82}O_{9-\delta}$ phase. On the basis of these phenomena and the variation in the $BaCoO_3$ peak observed via X-ray diffraction (XRD) after Nb doping, one possible explanation is that when Nb is present, Ba has a stronger tendency to form a $Ba_3Ca_{1.18}Nb_{1.82}O_{9-\delta}$ phase rather than a $BaCoO_3$ phase, but the amount of doped Nb is too small for the final formation of a mixture of the $Ba_3Ca_{1.18}Nb_{1.82}O_{9-\delta}$ phase and a slight $BaCoO_3$ phase in $PBCCN_{0.05}$.

The δ values of $PBCCN_{0.05}$ ($PrBa_{0.8}Ca_{0.2}Co_{1.95}Nb_{0.05}O_{6-\delta}$) and PBCC ($PrBa_{0.8}Ca_{0.2}Co_2O_{6-\delta}$) can be calculated according to the results of iodometric titration. Unexpectedly, δ of $PBCCN_{0.05}$ is 0.394, which is almost the same as that of PBCC (δ = 0.4). This phenomenon indicated that the Nb doping in $PBCCN_{0.05}$ had little effect on its oxygen vacancies at room temperature. The oxygen contents of the $PBCCN_{0.05}$ and PBCC samples at working temperatures (700–800 °C) were further characterized via thermogravimetric (TG) analysis. Figure 3 shows the TG analysis curves of the $PBCCN_{0.05}$ and PBCC samples in air from room temperature to 800 °C. An obvious weight loss occurred in both samples when the temperature reached approximately 300 °C, which can be attributed to the desorption of water and gases [41]. The weight loss from 300 to 800 °C should be related to the loss of lattice oxygen caused by the thermal reduction of variable-valent cations [42,43]. A greater weight loss is observed in $PBCCN_{0.05}$, as shown in Fig. 3, from approximately 300 to 800 °C, and its corresponding δ value of $PBCCN_{0.05}$ is 1.57 at 800 °C, whereas the δ value of PBCC is only 0.87 under the same conditions. The greater weight loss and higher δ of $PBCCN_{0.05}$ imply a higher concentration of oxygen vacancies, which is considered important for ORR to have more active sites at the working temperatures of SOFC. Therefore, it can be concluded that the concentration of oxygen vacancies in $PBCCN_{0.05}$ significantly increased after Nb doping at the working temperature of SOFC.

The apparent weight loss of 10% in the TG curve of $PBCCN_{0.05}$

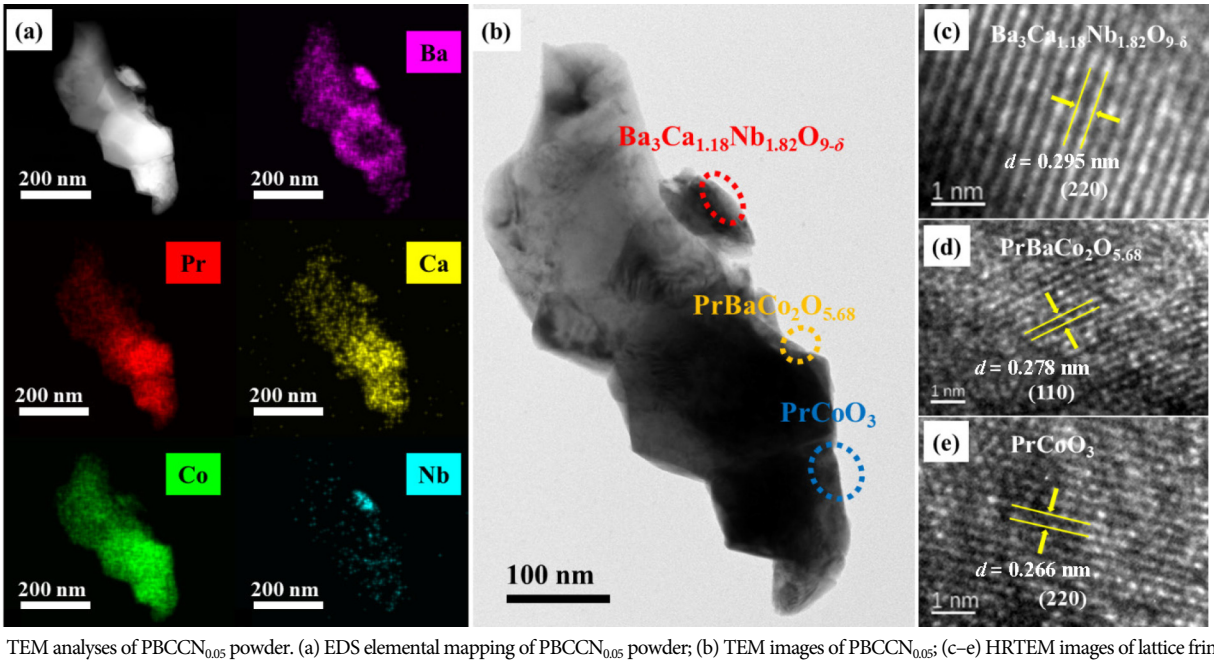

Fig. 2 TEM analyses of $PBCCN_{0.05}$ powder. (a) EDS elemental mapping of $PBCCN_{0.05}$ powder; (b) TEM images of $PBCCN_{0.05}$; (c–e) HRTEM images of lattice fringes in three marked areas.

清華大学出版社 Tsinghua University Press | SciOpen

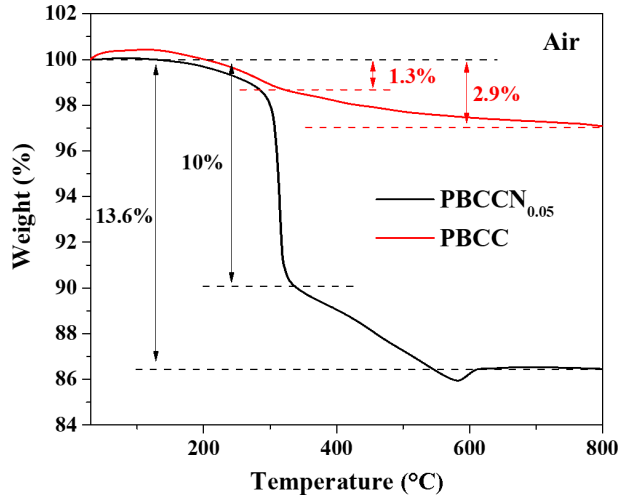

Fig. 3 TG analysis curves of $PBCCN_{0.05}$ and PBCC samples from room temperature to 800 °C at heating rate of 10 °C·min^{-1} in air.

at approximately 300 °C is also worth noticing because $PBCCN_{0.05}$ was calcined twice at 950 °C for 2 h during sample preparation, and there should be very little residual water in the $PBCCN_{0.05}$ sample before TG analysis. Therefore, most of the weight lost at approximately 300 °C in $PBCCN_{0.05}$ should theoretically be absorbed, and this inference is further discussed in the next XPS analysis (Fig. 4).

XPS analyses were used to understand the effect of Nb doping on the binding energy of the oxygen atoms in the PBCC and $PBCCN_{0.05}$. The measured XPS spectra are shown in Figs. 4(a) and 4(b). The ratio of the binding energy amount of the oxygen vacancy is calculated by deconvoluting the energy peak of the oxygen binding (O 1s) to obtain the oxygen vacancy ratio in PBCC and $PBCCN_{0.05}$. The deconvolution results in Fig. 4(a) show four kinds of oxygen species in both the PBCC and $PBCCN_{0.05}$ samples. The binding energy at approximately ~530 eV corresponds to the O_2^{2-}/O^- ions adsorbed by oxygen vacancies in the lattice at room temperature, which is likely related to the absorbed oxygen on the surface [44]. The O_2^{2-}/O^- ion peak (the purple peak) could be dependent on the concentration of oxygen vacancies. The O_2^{2-}/O^- ion peak of $PBCCN_{0.05}$ is greater than that of PBCC, which could be direct evidence of more oxygen being absorbed by $PBCCN_{0.05}$. The accurate ratio of each type of oxygen species is shown in Table 1. The ratio of O_2^{2-}/O^- increases from 21.84% in PBCC to 29.67% in $PBCCN_{0.05}$, indicating that more adsorbed gases are present in $PBCCN_{0.05}$ at approximately 300 °C. However, iodometric titration has shown that Nb doping in $PBCCN_{0.05}$ has little effect on its oxygen vacancies at room temperature. The absorbed oxygen in $PBCCN_{0.05}$ should not be attributed to its oxygen vacancies. The higher weight ratio of the $PrCoO_3$ perovskite phase in $PBCCN_{0.05}$ may play an important role because of its ability to improve oxygen adsorption/desorption, dissociation, and surface transport [45,46].

3.2 Symmetrical cell performance

To determine a suitable doping amount of Nb, four $PBCCN_x$ symmetrical cells with Nb doping amounts of x = 0, 0.025, 0.05, and 0.1 were fabricated. As shown in Figs. 5(a)–5(e), the EIS results of these four cathodes in ambient air at different temperatures indicate that $PBCCN_{0.05}$ has the lowest polarization resistance (R_p) among the samples. The R_p values of $PBCCN_{0.05}$ were 0.0074, 0.012, 0.022, and 0.054 Ω·cm^2 at 800, 750, 700, and 650 °C, respectively, which are better than those of PBCC (0.012, 0.020, 0.039, and 0.087 Ω·cm^2 at 800, 750, 700, and 650 °C, respectively. A 100-h stability test of the $PBCCN_{0.05}$ and PBCC cathodes at 700 °C in air under open-circuit voltage conditions is shown in Fig. 5(f). As shown in Fig. 5(f), both the $PBCCN_{0.05}$ and PBCC cathodes may have undergone an activation process during the stability test. The activation process lasted for 22 h in the $PBCCN_{0.05}$ cathode, and a longer activation process was observed for 48 h in the PBCC cathode. Rapid degradation can be observed in the PBCC cathode after the activation process, with a degradation rate of 4.81×10^{-5} Ω·cm^2·h^{-1}. In comparison, the degradation of the $PBCCN_{0.05}$ cathode is slower, with a lower degradation rate of 3.41×10^{-5} Ω·cm^2·h^{-1}, indicating that $PBCCN_{0.05}$ manifests better stability than PBCC after Nb doping. These results suggest that the doping of Nb can provide better stability and reduce R_p of the cathodes. As shown in Fig. 5(g), the thickness of the LSGM electrolyte for symmetrical cells is ~218 μm, and the $PBCCN_x$ electrodes on both sides of the symmetrical cell have similar thicknesses (8.43 and 11.9 μm). Further electrochemical

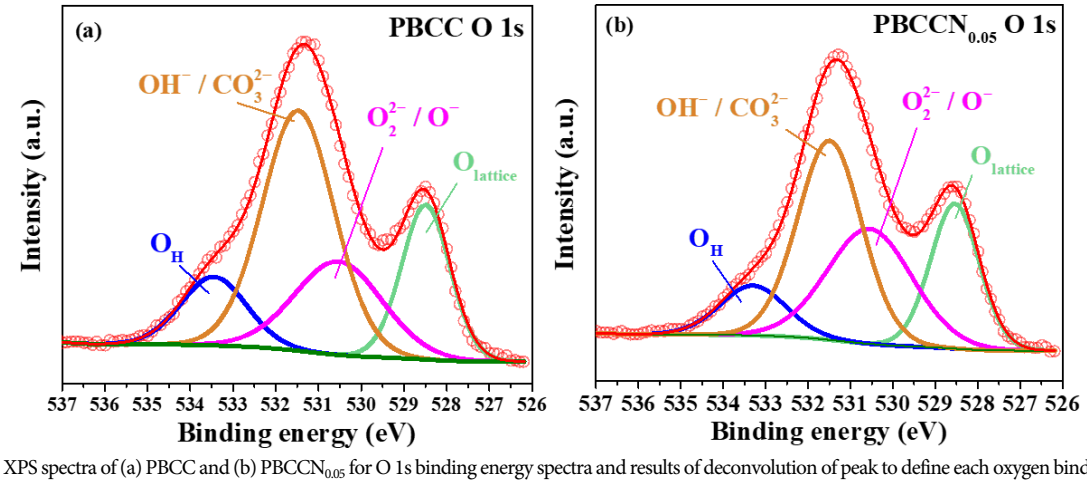

Fig. 4 XPS spectra of (a) PBCC and (b) $PBCCN_{0.05}$ for O 1s binding energy spectra and results of deconvolution of peak to define each oxygen binding type.

Table 1 Atomic percentages of four types of oxygen species in PBCC and $PBCCN_{0.05}$ cathode materials (Unit: at%)

	$O_{lattice}$	O_2^{2-}/O^-	OH^-/CO_3^{2-}	O_H	X^2
PBCC	19.96	21.84	46.17	12.03	1.2
$PBCCN_{0.05}$	21.47	29.67	38.85	10.02	1.6

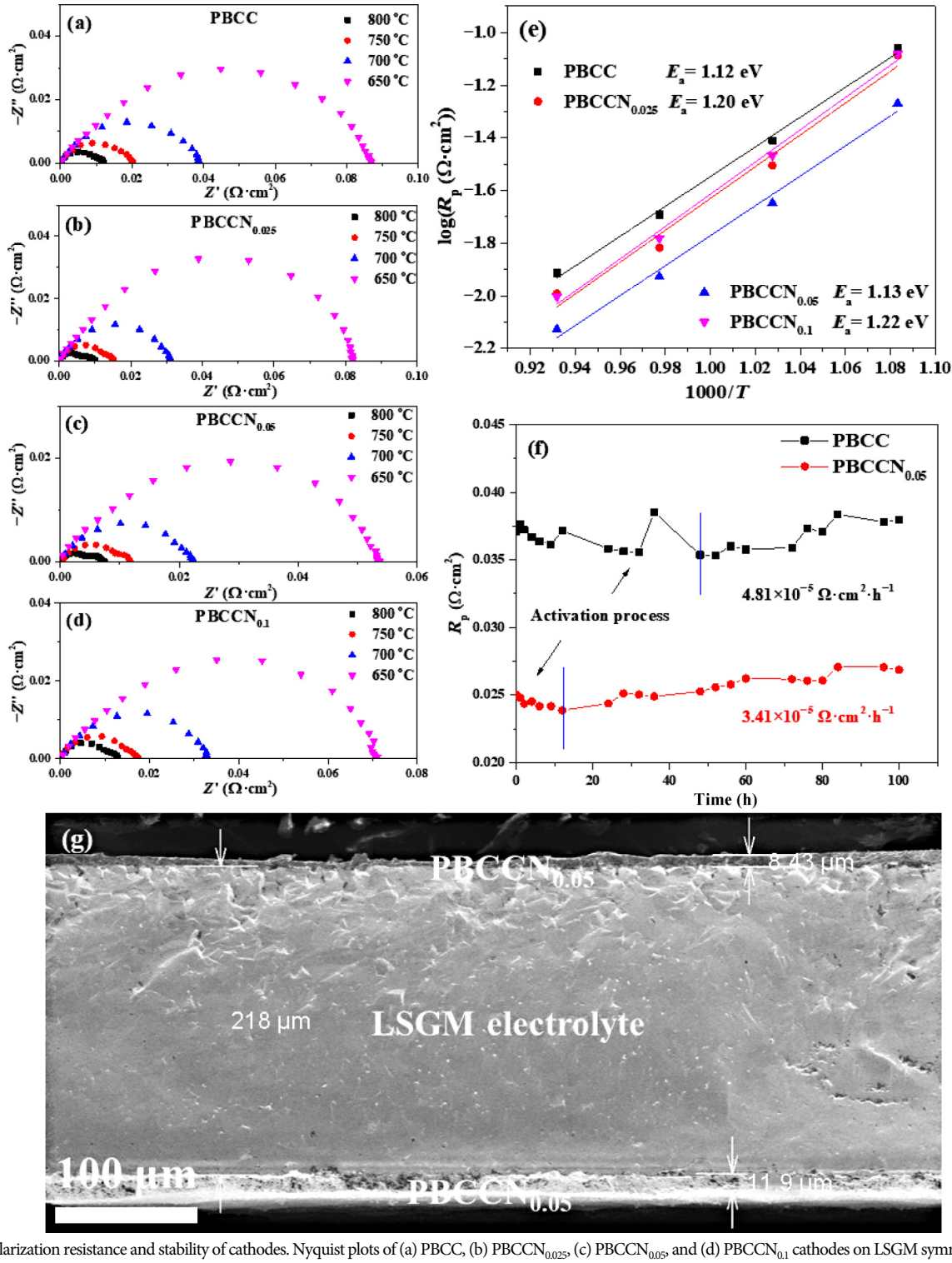

Fig. 5 Polarization resistance and stability of cathodes. Nyquist plots of (a) PBCC, (b) $PBCCN_{0.025}$, (c) $PBCCN_{0.05}$, and (d) $PBCCN_{0.1}$ cathodes on LSGM symmetrical cell between 650 and 800 °C in ambient air; (e) ASR and activation energy (E_a) of LSGM-based symmetrical cell with $PBCCN_x$ cathodes (x = 0, 0.025, 0.05, and 0.1) between 650 and 800 °C in air; (f) R_p of PBCC and $PBCCN_{0.05}$ cathodes in short-term stability test of 100 h at 700 °C in air; (g) SEM image of cross section in $PBCCN_{0.05}$ symmetrical cell with LSGM electrolyte.

testing, especially single-cell testing, is focused on the $PBCCN_{0.05}$ cathode since $PBCCN_{0.05}$ has the lowest R_p.

3.3 Symmetrical cells under oxygen partial pressure

The oxygen reduction reaction (ORR) is a complex process that includes multiple elementary reactions, including gas diffusion and molecular oxygen adsorption on the electrode surface, oxygen surface adsorption-dissociation, charge transfer, and oxygen ion migration from the electrode into the electrolyte [43]. By utilizing distribution of relaxation time (DRT) analysis, the total polarization resistance (R_p) of electrodes can be resolved into several R_p values for each elementary reaction. The relationship between these R_p values of the elementary reactions and the oxygen partial pressure (p_{O_2}) can be expressed by Eq. (1) [47]:

$$\frac{1}{R_p} \propto (p_{O_2})^n \quad (1)$$

Thus, the original elementary reaction of each R_p, as the rate-limiting step of ORR, can be identified by calculating its n value. All the elementary reactions and their corresponding n values have been studied [48] and are applied for the next discussion (Fig. 6).

To investigate how Nb doping in PBCCN$_x$ affects the ORR on the cathode, symmetrical cells of the PBCC and PBCCN$_{0.05}$ cathodes were tested under a N_2/O_2 atmosphere with a changing ratio of O_2 at 750 °C. The EIS data in Figs. 6(a) and 6(b) were further analyzed via DRT tools, as shown in Figs. 6(c) and 6(d). Two peaks can be found in both Figs. 6(c) and 6(d): one in the low-frequency (LF) area and one in the intermediate-frequency (IF) area. Notably, their peaks at low frequencies are similar, whereas the peak at intermediate frequencies decreases after Nb doping in PBCCN$_{0.05}$, implying a strong relationship between Nb doping and the IF peak. The n value of R_{LF} calculated from Fig. 6(f) is 1.09 (close to 1), and the n value of R_{IF} is 0.44 (close to 0.5) in the PBCC cathode, demonstrating that the original process of R_{LF} should be gas diffusion and molecular oxygen adsorption on the electrode surface [48,49], and the original process of R_{IF} should be oxygen surface adsorption-dissociation. Moreover, the n values of R_{LF} and R_{IF} calculated from Fig. 6(e) do not change much after Nb doping in PBCCN$_{0.05}$ (the n value of R_{LF} (n_L) is 1.24 ≈ 1, and the n value of R_{IF} (n_I) is 0.404 ≈ 0.5 in the PBCCN$_{0.05}$ cathode). This result may suggest that the rate-determining steps of ORR on the PBCCN$_{0.05}$ cathode remain unchanged after Nb doping. As the IF peak has a strong relationship with Nb doping, Nb doping in PBCCN$_{0.05}$ can affect the oxygen surface adsorption-dissociation step by decreasing the polarization resistance, thus increasing the ORR rate of the cathodes.

3.4 Single-fuel cell testing

The electrochemical performance of a single cell with a PBCCN$_{0.05}$ cathode was examined on a Ni–YSZ anode-supported cell with a thin YSZ electrolyte and a porous GDC buffer layer. A fuel cell with a PBCC cathode was also fabricated and tested for comparison. Figures 7(a)–7(d) show the typical IVP and EIS curves of the cells with the PBCCN$_{0.05}$ and PBCC cathodes. Figure 7(a) shows that the peak power density of the PBCCNb$_{0.05}$

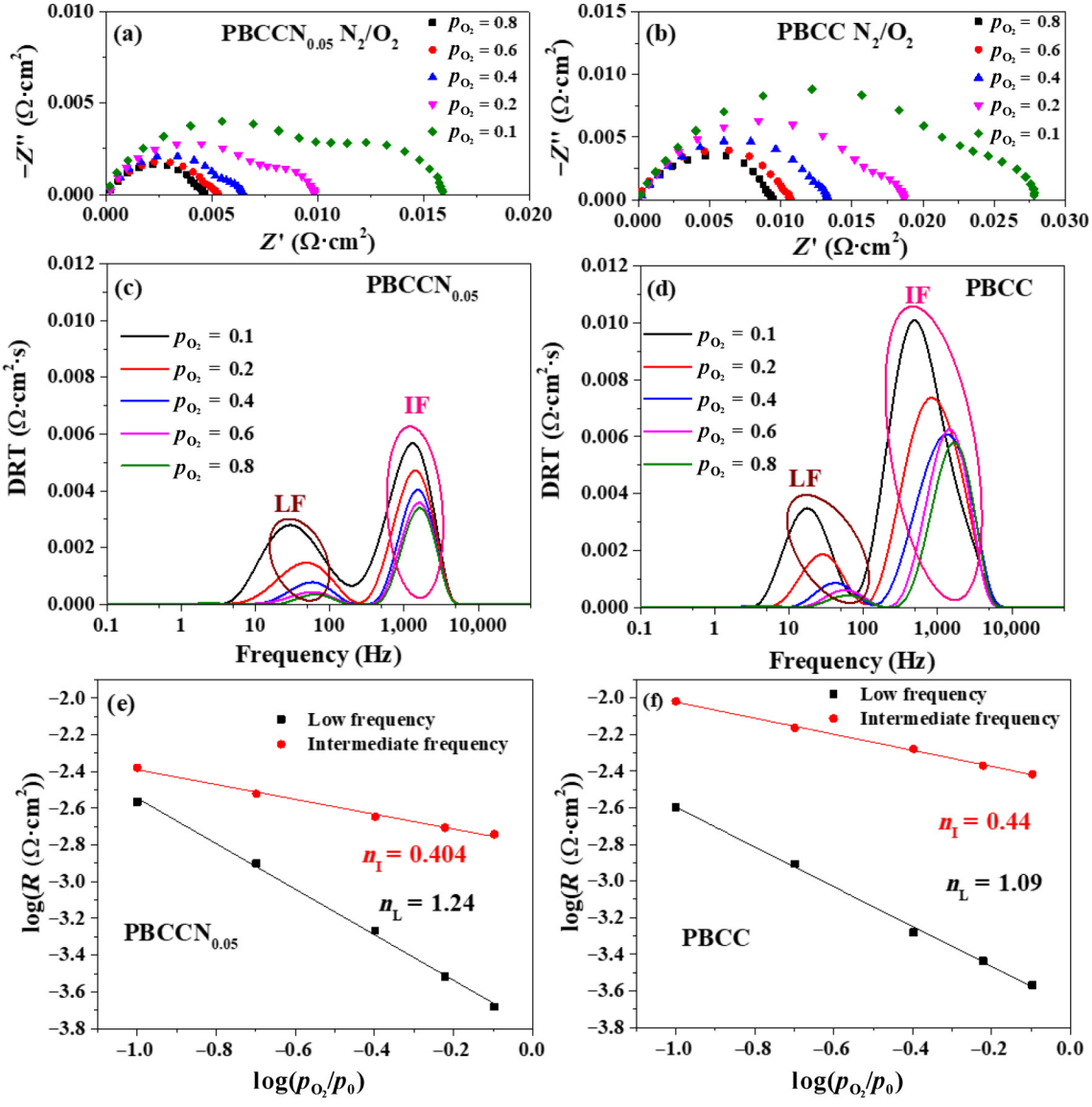

Fig. 6 Surface kinetics of PBCCN$_{0.05}$ and PBCC electrodes. Nyquist plots of (a) PBCCN$_{0.05}$ and (b) PBCC cathodes on LSGM-supported symmetrical cells; DRT curves of (c) PBCCN$_{0.05}$ and (d) PBCC cathodes; oxygen partial pressure dependence of polarization resistances (R) of (e) PBCCN$_{0.05}$ and (f) PBCC at 750 °C under oxygen partial pressures between 0.2 and 1.

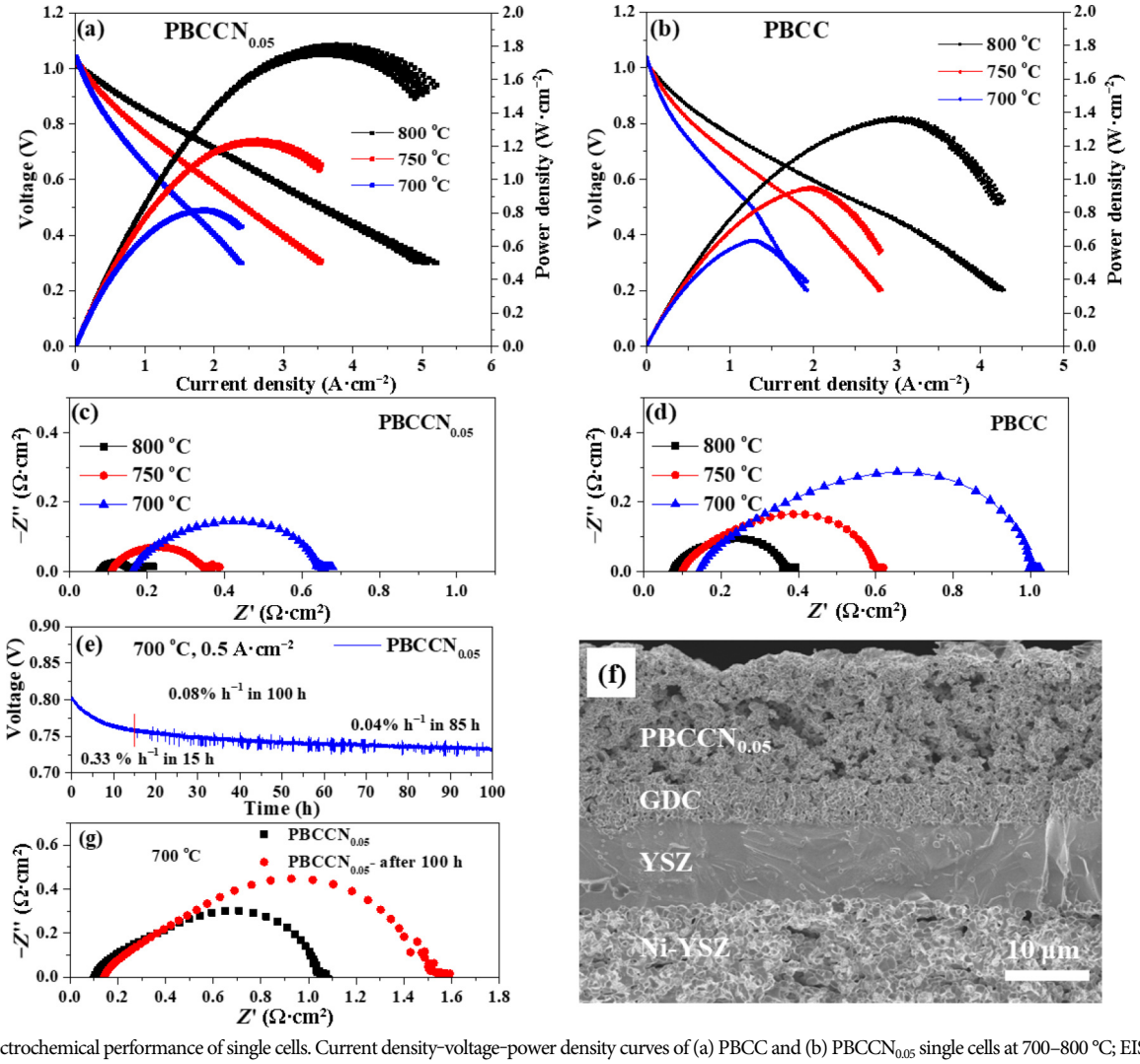

Fig. 7 Electrochemical performance of single cells. Current density–voltage–power density curves of (a) PBCC and (b) $PBCCN_{0.05}$ single cells at 700–800 °C; EIS of single cell with (c) PBCC and (d) $PBCCN_{0.05}$ cathodes at 700–800 °C; (f) SEM image of a section of Ni–YSZ/YSZ/GDC/$PBCCN_{0.05}$ single fuel cell after 100 h of short-term operation; (g) EIS of single cell with $PBCCN_{0.05}$ cathode at open-circuit potential before and after 100 h of short-term operation.

cell can reach 0.82, 1.23, and 1.81 W·cm^{-2} at 700, 750, and 800 °C, respectively, whereas the peak power density of the fuel cell with PBCC cathodes is only 0.64, 0.95, and 1.37 W·cm^{-2} at the same temperature, as shown in Fig. 7(b). This obvious improvement can also be reflected in the EIS results, as shown in Figs. 7(c) and 7(d). R_p of the $PBCCN_{0.05}$ cell is lower than that of the PBCC cell when the ohmic resistances of these two cells are similar at all the testing temperatures. These trends are consistent with the polarization resistances acquired from the symmetrical cell we tested above, suggesting that the ORR kinetics on the $PBCCN_{0.05}$ cathode accelerated after being doped with Nb. Figure 7(e) shows the short-term operation stability of the single cells with $PBCCN_{0.05}$ at 700 °C at a current density of 0.5 A·cm^{-2}. A rapid decrease in the $PBCCN_{0.05}$ voltage line (Fig. 7(e)) occurred during the first 15 h, with a degradation rate of 0.33% h^{-1}. The voltage then becomes stable and changes at a slow rate of decrease over the next 85 h, with a degradation rate of 0.04% h^{-1}. After 100 h of operation, the voltage of the $PBCCN_{0.05}$ single cell decreases from 0.8 to 0.73 V, and the degradation rate during the process is 0.08% h^{-1}. No obvious delamination or severe microstructural changes can be observed in the section of the fuel cell after 100 h of operation, as shown in Fig. 7(f), and the $PBCCN_{0.05}$ cathode is still in good contact with the GDC buffer layer. The main reason for the performance degradation of the single cell should not be the detachment of the $PBCCN_{0.05}$ cathode from the electrolyte. EIS of the single cell before and after 100 h of short-term operation in Fig. 7(g) indicates that the ohmic resistance changed from 0.1 to 0.14 Ω·cm^2, whereas R_p rose from 1.07 to 1.57 Ω·cm^2. The significantly increased R_p should be the key factor for the performance degradation of single cells. According to previous research [50], R_p of a single cell is affected by both the cathode and anode; however, the stability of the $PBCCN_{0.05}$ cathode has been proven in symmetrical cell experiments that the $PBCCN_{0.05}$ cathode should not be the main reason for the increase in R_p. The microstructural changes of the anode could cause a decrease in the performance of single cells.

4 Conclusions

We successfully synthesized the Nb-doped $PrBa_{0.8}Ca_{0.2}Co_2O_{6-\delta}$-based perovskite by a self-assembly method. The effects of Nb doping on the properties of the cathode of SOFCs have been investigated in symmetrical cells and single cells. A self-assembly phenomenon occurs on the precursor of PBCC during the 950 °C calcination step and forms a $PrCoO_3$-decorated $PrBaCo_2O_{5+\delta}$ phase with a few $BaCoO_3$ impurity phases. Nb doping in $PBCCN_{0.05}$ increases the ratio of the $PrCoO_3$ phase. Furthermore, Nb is not fully doped in the $PrCoO_3$ and $PrBaCo_2O_{5+\delta}$ phases; the

remaining Nb may further react to form a $Ba_3Ca_{1.18}Nb_{1.82}O_{9-\delta}$ phase. XPS analyses demonstrate that more oxygen vacancies are introduced into $PBCCN_{0.05}$ after Nb doping. Accordingly, the oxygen adsorption-dissociation step of ORR is accelerated on the $PBCCN_{0.05}$ surface, improving the ORR activity. The $PBCCN_{0.05}$ cathode has a low R_p of 0.0074 Ω·cm² in a symmetrical cell and a high peak power density of 1.81 W·cm^{-2} in a Ni–YSZ-supported single cell at 800 °C. Furthermore, it also demonstrated reasonable short-term operation stability.

Acknowledgements

This work was financially supported by the Introduced Innovative R&D Team of Guangdong (No. 2021ZT09L392), the National Natural Science Foundation of China (Nos. 22179039 and 22005105), the Pearl River Talent Recruitment Program (No. 2019QN01C693), and the Natural Science Foundation of Guangdong Province (No. 2021A1515010395).

Declaration of competing interest

The authors have no competing interests to declare that are relevant to the content of this article.

Electronic Supplementary Material

Supplementary material is available in the online version of this article at https://doi.org/10.26599/JAC.2024.9220959.

References

[1] Bian WJ, Wu W, Wang BM, *et al.* Revitalizing interface in protonic ceramic cells by acid etch. *Nature* 2022, **604**: 479–485.
[2] Yu YF, You QL, Zuo ZY, *et al.* Compound climate extremes in China: Trends, causes, and projections. *Atmos Res* 2023, **286**: 106675.
[3] Bolan S, Padhye LP, Jasemizad T, *et al.* Impacts of climate change on the fate of contaminants through extreme weather events. *Sci Total Environ* 2024, **909**: 168388.
[4] Aguir Bargaoui S, Nouri FZ. History of the human and nature relationship, discovery of greenhouse effect and awareness of the environmental problem. *J Tecon Sci Res* 2021, **4**: 23–34.
[5] Ranta A, Kang J, Saad A, *et al.* Climate change and stroke: A topical narrative review. *Stroke* 2024, **55**: 1118–1128.
[6] Jackson RB, Friedlingstein P, Le Quéré C, *et al.* Global fossil carbon emissions rebound near pre-COVID-19 levels. *Environ Res Lett* 2022, **17**: 031001.
[7] Vohra K, Vodonos A, Schwartz J, *et al.* Global mortality from outdoor fine particle pollution generated by fossil fuel combustion: Results from GEOS-Chem. *Environ Res* 2021, **195**: 110754.
[8] Sharma V, Tsai ML, Nargotra P, *et al.* Journey of lignin from a roadblock to bridge for lignocellulose biorefineries: A comprehensive review. *Sci Total Environ* 2023, **861**: 160560.
[9] Sirohi R, Vivekanand V, Pandey AK, *et al.* Emerging trends in role and significance of biochar in gaseous biofuels production. *Environ Technol Innov* 2023, **30**: 103100.
[10] Sharma VK, Singh R, Gehlot A, *et al.* Imperative role of photovoltaic and concentrating solar power technologies towards renewable energy generation. *Int J Photoenergy* 2022, **2022**: 3852484.
[11] Roga S, Bardhan S, Kumar Y, *et al.* Recent technology and challenges of wind energy generation: A review. *Sustain Energy Technol Assess* 2022, **52**: 102239.
[12] Li G, Zhu WD. Tidal current energy harvesting technologies: A review of current status and life cycle assessment. *Renew Sust Energ Rev* 2023, **179**: 113269.
[13] Hauch A, Ploner A, Pylypko S, *et al.* Test and characterization of reversible solid oxide cells and stacks for innovative renewable energy storage. *Fuel Cells* 2021, **21**: 467–476.
[14] Agbaje MA, Akkaya AV. Electrochemical-energy- exergy analysis of reversible solid oxide cell-based small-scale stand-alone energy storage system. *Case Stud Therm Eng* 2023, **52**: 103732.
[15] Aicart J, Di Iorio S, Petitjean M, *et al.* Transition cycles during operation of a reversible solid oxide electrolyzer/fuel cell (rSOC) system. *Fuel Cells* 2019, **19**: 381–388.
[16] Choudhury A, Chandra H, Arora A. Application of solid oxide fuel cell technology for power generation—A review. *Renew Sust Energ Rev* 2013, **20**: 430–442.
[17] Akikur RK, Saidur R, Ping HW, *et al.* Performance analysis of a co-generation system using solar energy and SOFC technology. *Energy Convers Manage* 2014, **79**: 415–430.
[18] Ndubuisi A, Abouali S, Singh K, *et al.* Recent advances, practical challenges, and perspectives of intermediate temperature solid oxide fuel cell cathodes. *J Mater Chem A* 2022, **10**: 2196–2227.
[19] Jun A, Kim J, Shin J, *et al.* Perovskite as a cathode material: A review of its role in solid-oxide fuel cell technology. *ChemElectroChem* 2016, **3**: 511–530.
[20] Li ZH, Li MR, Zhu ZH. Perovskite cathode materials for low-temperature solid oxide fuel cells: Fundamentals to optimization. *Electrochem Energy Rev* 2022, **5**: 263–311.
[21] Sunarso J, Hashim SS, Zhu N, *et al.* Perovskite oxides applications in high temperature oxygen separation, solid oxide fuel cell and membrane reactor: A review. *Prog EnergCombust* 2017, **61**: 57–77.
[22] Tarutin AP, Filonova EA, Ricote S, *et al.* Chemical design of oxygen electrodes for solid oxide electrochemical cells: A guide. *Sustain Energy Technol Assess* 2023, **57**: 103185.
[23] Jiang SP. Development of lanthanum strontium cobalt ferrite perovskite electrodes of solid oxide fuel cells–A review. *Int J Hydrog Energ* 2019, **44**: 7448–7493.
[24] Yu H, Kim SG, Im HN, *et al.* Uniform and scalable Sm^{3+} and Nd^{3+} doped ceria nanocatalysts decorating bifunctional oxygen electrodes for high performing reversible solid oxide electrochemical cells. *Chem Eng J* 2023, **475**: 146002.
[25] Jia W, Wang Y, Huang J, *et al.* Alternative B-site-doped $La_{0.6}Sr_{0.4}Co_{0.2}Fe_{0.8-x}M_xO_3$ (M = Ni, Cu, Nb; x = 0, 0.1, 0.2) as innovative cathode material for LT-SOFC with enhanced charge transfer and oxygen ion diffusion. *Appl Energ* 2024, **353**: 122096.
[26] Zhou W, Ran R, Shao ZP. Progress in understanding and development of $Ba_{0.5}Sr_{0.5}Co_{0.8}Fe_{0.2}O_{3-\delta}$-based cathodes for intermediate-temperature solid-oxide fuel cells: A review. *J Power Sources* 2009, **192**: 231–246.
[27] Sahini MG, Mwankemwa BS, Kanas N. $Ba_xSr_{1-x}Co_yFe_{1-y}O_{3-\delta}$ (BSCF) mixed ionic-electronic conducting (MIEC) materials for oxygen separation membrane and SOFC applications: Insights into processing, stability, and functional properties. *Ceram Int* 2022, **48**: 2948–2964.
[28] Sun SC, Cheng Z. Effects of H_2O and CO_2 on electrochemical behaviors of BSCF cathode for proton conducting IT-SOFC. *J Electrochem Soc* 2016, **164**: F81–F88.
[29] Zhu L, Wei B, Lü Z, *et al.* Performance degradation of double-perovskite $PrBaCo_2O_{5+\delta}$ oxygen electrode in CO_2 containing atmospheres. *Appl Surf Sci* 2017, **416**: 649–655.
[30] Kim G, Wang S, Jacobson AJ, *et al.* Rapid oxygen ion diffusion and surface exchange kinetics in $PrBaCo_2O_{5+x}$ with a perovskite related structure and ordered A cations. *J Mater Chem* 2007, **17**: 2500–2505.
[31] Hu T, Xu YS, Xu K, *et al.* Visiting the roles of Sr- or Ca- doping on the oxygen reduction reaction activity and stability of a perovskite cathode for proton conducting solid oxide fuel cells. *SusMat* 2023, **3**: 91–101.
[32] Zhu F, He F, Xu K, *et al.* Enhancing the oxygen reduction reaction activity and durability of a double-perovskite via an A-site tuning. *Sci China Mater* 2022, **65**: 3043–3052.
[33] Xu K, Zhang H, Xu YS, *et al.* An efficient steam-induced heterostructured air electrode for protonic ceramic electrochemical cells. *Adv Funct Mater* 2022, **32**: 2110998.
[34] Xu K, Zhang H, Xu YS, *et al.* Phase engineering of a donor-doped air

electrode for reversible protonic ceramic electrochemical cells. *Adv Powder Mater* 2024, **3**: 100187.
[35] Jin FJ, Liu XW, Tian YF, *et al.* Enhancing oxygen reduction activity and CO_2 tolerance by a bismuth doping strategy for solid oxide fuel cell cathodes. *Adv Funct Mater* 2024, **34**: 2400519.
[36] Chen Y, Yoo S, Choi Y, *et al.* A highly active, CO_2-tolerant electrode for the oxygen reduction reaction. *Energ Environ Sci* 2018, **11**: 2458–2466.
[37] Lim C, Sengodan S, Jeong D, *et al.* Investigation of the Fe doping effect on the B-site of the layered perovskite $PrBa_{0.8}Ca_{0.2}Co_2O_{5+\delta}$ for a promising cathode material of the intermediate-temperature solid oxide fuel cells. *Int J Hydrog Energ* 2019, **44**: 1088–1095.
[38] Zhang Y, Shen LY, Wang YH, *et al.* Enhanced oxygen reduction kinetics of IT-SOFC cathode with $PrBaCo_2O_{5+\delta}/Gd_{0.1}Ce_{1.9}O_{2-\delta}$ coherent interface. *J Mater Chem A* 2022, **10**: 3495–3505.
[39] Zhou YC, Liu EZ, Chen Y, *et al.* An active and robust air electrode for reversible protonic ceramic electrochemical cells. *ACS Energy Lett* 2021, **6**: 1511–1520.
[40] Gu HX, Yang GM, Hu Y, *et al.* Enhancing the oxygen reduction activity of $PrBaCo_2O_{5+\delta}$ double perovskite cathode by tailoring the calcination temperatures. *Int J Hydrog Energy* 2020, **45**: 25996–26004.
[41] Zhang LL, Yao GB, Song ZY, *et al.* Effects of Pr-deficiency on thermal expansion and electrochemical properties in $Pr_{1-x}BaCo_2O_{5+\delta}$ cathodes for IT-SOFCs. *Electrochim Acta* 2016, **212**: 522–534.
[42] Li M, Li H, Jiang XC, *et al.* Gd-induced electronic structure engineering of a NiFe-layered double hydroxide for efficient oxygen evolution. *J Mater Chem A* 2021, **9**: 2999–3006.
[43] He F, Hou MY, Liu DL, *et al.* Phase segregation of a composite air electrode unlocks the high performance of reversible protonic ceramic electrochemical cells. *Energy Environ Sci* 2024, **17**: 3898–3907.
[44] Yin YR, Zhou YB, Gu YY, *et al.* Successful preparation of $BaCo_{0.5}Fe_{0.5}O_{3-\delta}$ cathode oxide by rapidly cooling allowing for high-performance proton-conducting solid oxide fuel cells. *J Adv Ceram* 2023, **12**: 587–597.
[45] Li J, Zhou X, Wu CC, *et al.* Self-stabilized hybrid cathode for solid oxide fuel cell: A-site deficient perovskite coating as solid solution for strontium diffusion. *Chem Eng J* 2022, **438**: 135446.
[46] Chen Y, Choi Y, Yoo S, *et al.* A highly efficient multi-phase catalyst dramatically enhances the rate of oxygen reduction. *Joule* 2018, **2**: 938–949.
[47] Choi SM, An H, Yoon KJ, *et al.* Electrochemical analysis of high-performance protonic ceramic fuel cells based on a columnar-structured thin electrolyte. *Appl Energ* 2019, **233**: 29–36.
[48] Shen LY, Du ZH, Zhang Y, *et al.* Medium-Entropy perovskites $Sr(Fe_\alpha Ti_\beta Co_\gamma Mn_\zeta)O_{3-\delta}$ as promising cathodes for intermediate temperature solid oxide fuel cell. *Appl Catal B Environ* 2021, **295**: 120264.
[49] Zhu F, Xu K, He F, *et al.* An active and contaminants-tolerant high-entropy electrode for ceramic fuel cells. *ACS Energy Lett* 2024, **9**: 556–567.
[50] Wang YD, Marchetti B, Zhou XD. Call attention to using DRT and EIS to quantify the contributions of solid oxide cell components to the total impedance. *Int J Hydrog Energ* 2022, **47**: 35437–35448.